From atom level to macroscopic scale: structural mechanism of gypsum dehydration

Florian Beaugnon, João G D Preturlan, Florian Fusseis, Emmanuelle Gouillart, Sara Quiligotti, Gilles Wallez

From atom level to macroscopic scale: structural mechanism of gypsum dehydration

Florian Beaugnon [a,b,c], João G. D. Preturlan [d,e], Florian Fusseis [f], Emmanuelle Gouillart [c], Sara Quiligotti [e], Gilles Wallez [a,b,g,*]

[a] Chimie ParisTech, PSL Research University, CNRS, Institut de Recherche de Chimie Paris (IRCP), CNRS UMR 8247, 75005 Paris, France
[b] Centre de Recherche et de Restauration des Musées de France (C2RMF), Ministère de la Culture et de la Communication, 14, quai François Mitterrand, 75001 Paris, France
[c] Joint Unit CNRS/Saint-Gobain, Surface du Verre et Interfaces (SVI), 39 quai Lucien Lefranc, 93000 Aubervilliers, France
[d] Mines Saint-Etienne, Université de Lyon, CNRS, UMR 5307 LGF, Centre SPIN, 42023 Saint-Etienne, France
[e] Saint-Gobain Research Paris, 39 quai Lucien Lefranc, 93000 Aubervilliers, France
[f] School of Geosciences, University of Edinburgh, Edinburgh, UK
[g] UFR 926, Sorbonne Université, 75005 Paris, France

*corresponding author: gilles.wallez@sorbonne-universite.fr

Highlights

- First study of gypsum single crystal dehydration using X-ray absorption tomography
- Evidence and mechanism of a multi-scale crack pattern due to structure change
- How stress-induced shearing generates the “fishbone“ patterns

Abstract

Plaster, made of calcium sulfate hemihydrate ($CaSO_4$•½H_2O) and/or *γ*-anhydrite ($CaSO_4$) is obtained by dehydration of gypsum ($CaSO_4$•2H_2O) at 100-200 °C. When mixed with water, it dissolves while new gypsum crystals precipitate. Plaster’s microstructures affect its reactivity and setting properties, but are poorly understood due to confusion between crystals and polycrystalline structures in the literature. Through a multi-scale approach combining X-ray microtomography, optical and scanning electron microscopy, we revealed size, morphology and orientation of pores and crystals formed by dehydrating single crystals at T = 105-130 °C and p_{H2O} = 0-40 hPa. The expulsion of water from the (010) interlayers results in a three-level fragmentation: cracks form parallel to (010), then the solid is divided into [101] polycrystalline needles (5-10 x 30-300 µm) formed of micron-sized crystals arranged in a fishbone pattern. The same behavior is observed whatever T and p_{H2O}, however the crystallites size increases with p_{H2O}.

Graphical abstract

Gypsum dehydration-induced microstructure: the fishbone pattern is the smallest feature in a multi-scale system of cracks induced by strains in the crystal structure.

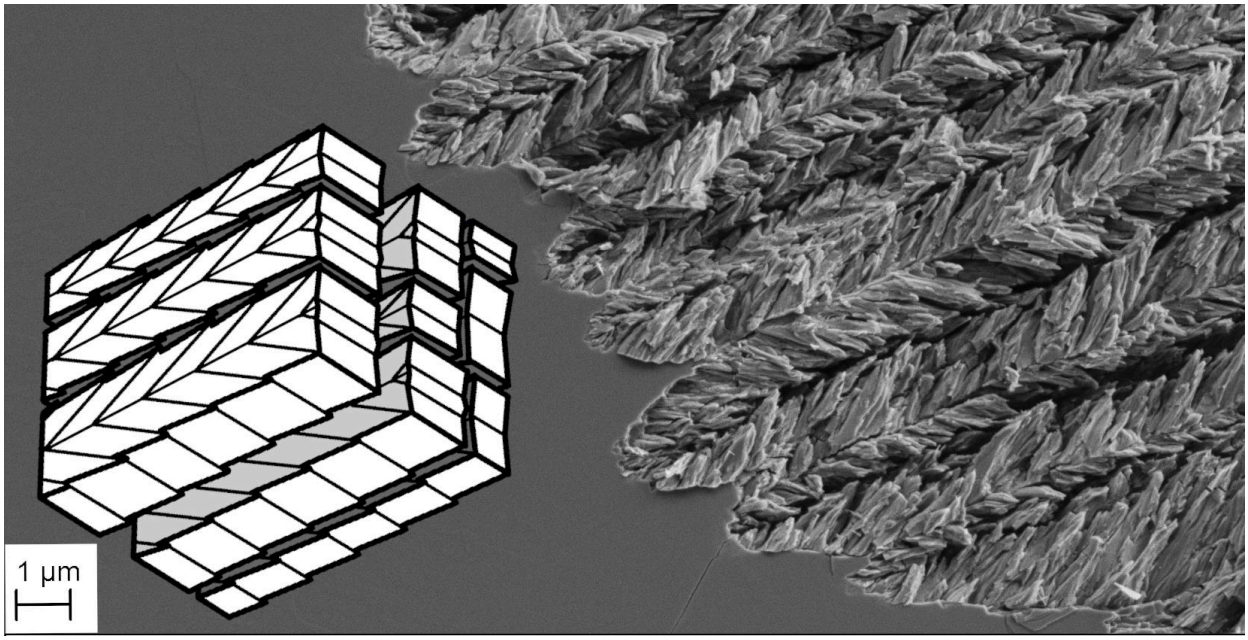

Keywords

- gypsum dehydration
- X-ray absorption tomography
- microstructure

1. Introduction

1.1 General context

Gypsum plaster is an inorganic binder that is prepared in a two-step process. The first step is dehydration: heated to 100-200 °C, gypsum ($CaSO_4•2H_2O$) releases water as vapor [1,2] and, depending on temperature and water vapor partial pressure (p_{H2O}) [3,4] forms either hemihydrate ($CaSO_4•½H_2O$) or *γ*-anhydrite ($CaSO_4$), the main components of the reactive plaster powder. When mixed with water and left to set in the second step of the transformation, these two highly soluble compounds dissolve to saturation, thus leading to the precipitation and growth of neoformed gypsum crystals [5,6].

1.2 Crystal structures, dehydration mechanism and microstructures

As stressed by Follner *et al.* [7] the crystal structures of gypsum [8-10], hemihydrate [11-13] and *γ*-anhydrite [11,14,15] have been the object of numerous, but often divergent publications. Actually, although these models only differ in minor details regarding atomic positions, they are based on a confusing variety of space groups and unit cells. In the present work, we will refer to the data reported by Pedersen *et al*. for gypsum (monoclinic, space group $I2_1/a$) [8] and Bezou *et al.* for *γ*-anhydrite (orthorhombic, *C*222) [11] which take into account minor cell distortions. In the following, the *G* and *A* subscripts for the crystal axes and planes will refer to these materials.

Gypsum is made up of alternate planes of water and calcium sulfate stacked along $[010]_G$ (Fig. 1). The latter are, in turn, made up of $[101]_G$ Ca-SO_4- chains (Fig. 2) which are

preserved during dehydration [16]. Parallel to the $[001]_A$ axis of γ-anhydrite and hemihydrate, they form a honeycomb structure in which the remaining $½H_2O$ molecule of the hemihydrate is hosted.

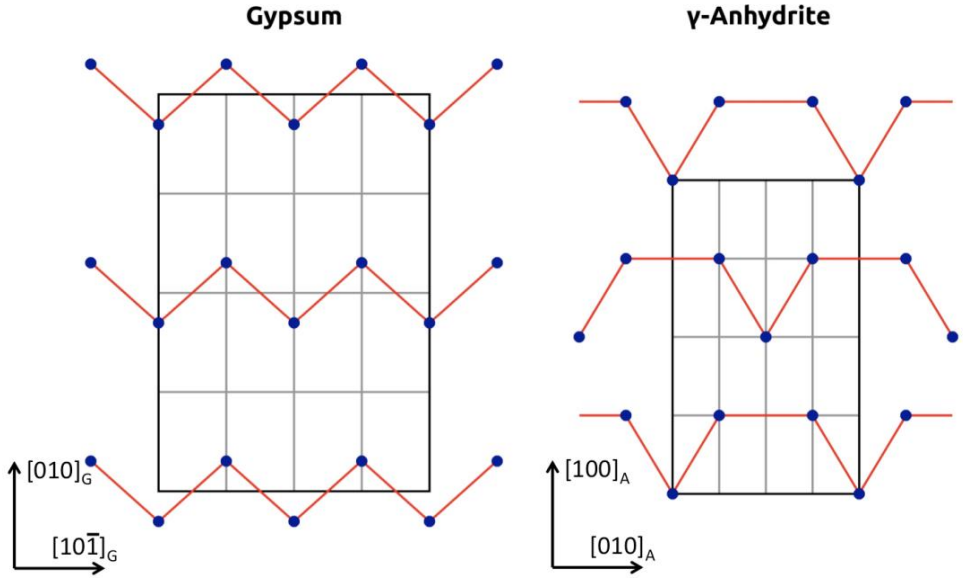

Fig. 1. Schematic view down the Ca-SO_4- chains (blue dots) of the crystal structures of gypsum [8] and γ-anhydrite [11]. Inter-chains Ca-O bonds forming close-packed layers are indicated in red, evidencing a contraction along $[010]_G$ and $[10\text{-}1]_G$ due to dehydration.

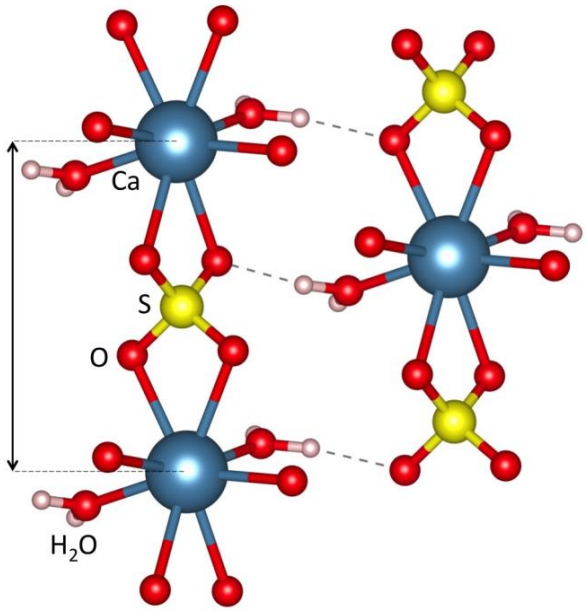

Fig. 2. Tilted (010) view of two Ca-SO_4- chains linked by hydrogen bonds in gypsum [8]. Chain's period corresponds to the arrow. Artwork made with Vesta [20].

As the structures of hemihydrate and *γ*-anhydrite are remarkably similar, the dehydration of gypsum into one or the other follows the same mechanisms with regard to structural and microstructural modifications [21,22]. The reaction involves a strong reconstruction of the crystal structure with marked modifications of the cell dimensions:
- as a direct steric effect of water loss, the $[010]_G$ interlayer spacing shrinks by 20.6%, resulting in wide cracks dividing the dehydrated gypsum crystals into smaller particles, forming complex microstructures. The transformation is topotactic, and both crystals and cracks follow discrete orientations relative to the structure of gypsum due to the preservation of Ca-SO_4- chains [16].
- the deformation of the layers results in a 11.4% contraction along $[10\text{-}1]_G$; to our knowledge, this less straightforward consequence of dehydration has not yet been analyzed.
- besides, the transformation of the Ca-OH_2---O-(Ca,S) interchain linkage (Fig. 2) into Ca-O-(Ca,S) leads to a change in the coordination of calcium, from $CaO_6(H_2O)_2$ in gypsum to CaO_8 in anhydrite. A survey of the “recent“ crystallographic data available for the two phases (see Supplementary Information) reveals a stretching of the chain periodicity, from 6.274-6.283 Å to 6.300-6.304 Å. Despite being small (0.3 to 0.5 %), this expansion can be seen as unambiguous as its calculation is based purely on the cell parameters. Conversely, the origin of the phenomenon could only be ascertained by analyzing the variations of the bond lengths and angles, but unfortunately, the variability of bond length and angles reported in the literature doesn't allow to confirm this assumption. So far, we can only speculate that the replacement of two “weak“ Ca-(OH_2) bonds in equatorial position by two “strong“ Ca-O ones induces a weakening - therefore a lengthening - of the intra-chain Ca-O bonds. Whatever the origin, the global stretching of the chains must be taken into account in the analysis of the microstructural transformations.

1.3 Pending issues

The microstructure of dehydrated gypsum is a key feature as the release of water vapor through the network of percolating shrinkage cracks can control the rate of the dehydration process [17]. In addition, it affects the ability of plaster to re-hydrate as well as its mechanical properties after setting [18]. However, it is currently difficult to propose a comprehensive description of the microstructures based on the various published results due to some contradictions between them.

Various crystal sizes and morphologies have been reported in the literature. Fowler observed "hourglass" patterns with a typical size of 10 µm using optical microscopy [19]. Nanometer-sized needles along $[101]_G$ have been conjectured in [23] based on electron microdiffraction experiments and previous observations of nm-scaled structures [16,24]. These results conflict with the report of crystals arranged in "fishbone" patterns with a typical size of 1 µm along $[101]_G$ that were observed by electron microscopy [25]. Cracks have not garnered as much attention as crystal morphologies but it is known that they follow a limited number of discrete orientations along planes of high atomic density. They have been reported to be self-similar across several orders of magnitude down to the nanometer [16].

These seemingly antagonistic results are difficult to compare as various authors report on distinct phenomena observed on samples (single- or polycrystals) prepared under a wide range of temperature, pressure and partial water vapor pressure conditions that can conceivably result in marked differences in behavior.

Indeed, these three parameters affect the microstructures formed by the dehydration of gypsum. Two main microstructural varieties called *α* and *β* (not to be confused with *α*-, *β*- and *γ*-anhydrite) are defined according to the plaster processing conditions. Dehydration in a dry atmosphere leads to the formation of *β*-plasters characterized by small crystal size and high

specific surface, while *α*-plasters prepared by dehydration in a wet atmosphere or by hydrothermal processes show larger crystal size and lower specific surface [18]. Most published studies report on microstructures observed in *β*-plasters, but even within ranges of temperature and p_{H2O} leading to the formation of *β*-plasters, both the shapes and sizes of structures have been found to be affected by these two parameters [18,25].

It is also worth noting that every previous model has been proposed on the basis of 2D measurements, which only allow a partial observation of three-dimensional microstructures.

1.4. Objectives

The purpose of this work is to improve our understanding of the microstructures formed by the dehydration of gypsum, for a set of well-controlled conditions. The main objectives are:

- to characterize the sizes, morphologies and orientation of cracks, crystals and larger polycrystalline structures found in dehydrated gypsum, on scales ranging from the nm to the mm;
- to explain the mechanisms of microstructural modifications;
- to compare samples dehydrated under controlled conditions of *T* and p_{H2O} to study their effect on the microstructures' sizes and morphologies.

The kinetic analysis of the present study is also an interesting aspect worth investigating and it will be the topic of a future publication. The X-ray microtomography experiments were conducted in-situ to monitor both the progress of the reaction and the microstructural transformations in real time. They were supplemented with optical and scanning electron microscopy ex-situ imaging of dehydrated samples for microstructural analysis on a wider range of scale.

2. Experimental

2.1 Materials and thermal treatment

Samples were taken from a transparent single crystal of gypsum (selenite) mined in Oxfordshire, UK. They were prepared by a combination of cleaving and cutting with a scalpel in the shape of a square prism (3 to 5 mm along $[100]_G$, 0.5 to 1 mm along $[010]_G$ and $[001]_G$; the orientation of crystals was identified from cleaving directions [26]). In addition, cut samples were etched in distilled water at 60 °C under stirring for a few minutes to remove possible surface asperities, with the side effect of rounding off the corners (fig. 4).

Dehydration experiments were conducted in a custom-made gas flow furnace supplied by Edinburgh Geoscience Microtomography at the University of Edinburgh to dehydrate the samples under controlled temperature and humidity conditions. Partial water vapor pressure in the nitrogen carrier gas flow was controlled by a two-part homemade apparatus [27]. Nitrogen was first bubbled in a Schlenk flask filled with water at 60 °C, generating water vapor with a partial pressure near saturation conditions (200 hPa). The gas flow was then cooled down in a condensing column connected to a thermostat bath to set a lower, controlled dew point. All tubing leading from the water vapor generator to the furnace was heated to avoid condensation in the gas path. Water vapor partial pressure values were calibrated and controlled for stability with a coupled hygrometer at the exit of the system. The 1 L/min gas flow was fed at the bottom of the furnace, heated by an electric heating element before exiting at the top of the furnace. There, it flowed through a polyimide chamber (transparent to X-rays) in which the sample was enclosed and glued on a sample holder. A type-K thermocouple in the sample holder was put in direct contact with the sample to measure the local temperature.

Temperatures measured by the sample thermocouple ranged from 105 to 130 °C, and water vapor partial pressures from 0 to 40 hPa, leading to the formation of *γ*-anhydrite, according to the phase diagram for this system [4].

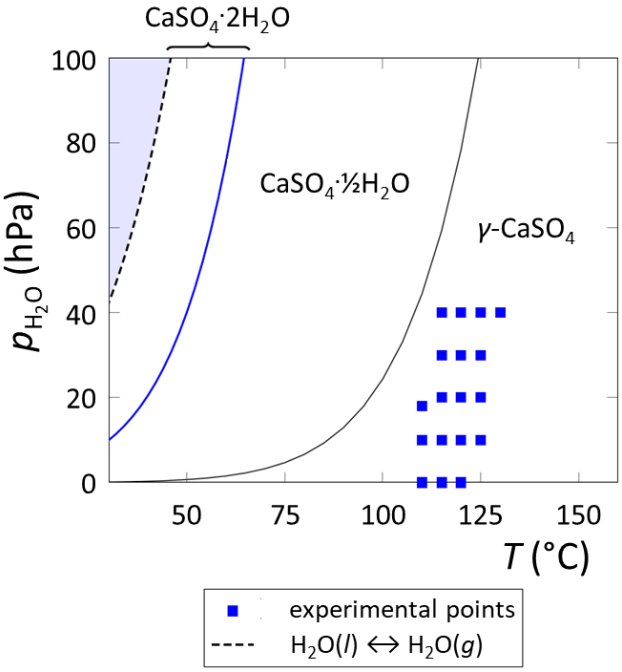

Fig. 3. Experimental points plotted in the pressure-temperature phase diagram of the $CaSO_4$-H_2O system, drawn after [4]

2.2 Acquisition and reconstruction of images

Experiments were conducted at the ESRF synchrotron micro-tomography beamline ID19 [28,29]. The choice of the source was motivated by the need for high-resolution imaging, combined with the short acquisition time required to study the kinetics of dehydration.

The volumes were modeled with 0.65^3 µm^3 voxels on the basis of 2000 radiographies acquired over a 180° angular range over 2 min with a sCMOS PCO Edge camera. A pink beam with 19.6 keV peak energy was used, and the transmitted X-rays were converted to visible light by a 10 µm GGG scintillator set at 33 mm from the sample to limit phase contrast. The image acquisition was reapeated continuously over the course of experiments to record time series.

X-ray absorption maps were reconstructed in three dimensions from the raw data using the PyHST algorithm [30] and processed with the Python package Scikit-image [31,32].

2.3 Measurement of the typical size of microstructures

The typical size of microstructures in dehydrated gypsum is close to the instrumental resolution. Therefore, slight differences in typical size between samples can fall below voxel size, making them impossible to measure directly on images or through an autocorrelation function. The dispersion of X-ray absorption values was instead used as an indirect indicator of typical size for comparison purposes. Indeed, dehydrated areas are only made up of anhydrite and pores. This means that the measured value of the X-ray absorption coefficient only depends on the proportion of anhydrite and pores in the sampled volume over which it is

averaged (the voxel); and that there is a positive correlation between the typical size of microstructures and the dispersion of the coefficient of absorption measured at constant sampling size.

For each experiment, local absorption values after dehydration were recorded on three image slices across the sample height. They are scattered around the average value in a single peak, whose full width at half-height was recorded.

2.4 Post-mortem imaging

Partially dehydrated samples were observed post-mortem. Micrographs were taken on both the outer $(010)_G$ surfaces (optical microscopy, Olympus SZX9) and on internal $(010)_G$ surfaces revealed by cleaving (scanning electron microscopy, Zeiss SUPRA 55VP).

3. Results and discussion

3.1 Description of microstructures

The tomographic images recorded correspond to 3D X-ray absorption maps: illustrations in Fig. 4 show regions with low absorption coefficients in darker shades of grey and high absorption coefficients in lighter shades. There is a clear contrast between calcium sulfate and air, but not between gypsum and anhydrite due to their similar compositions. However, the growth of porosity makes it easy to identify dehydrated areas. Even cracks that are narrower than voxel size result in a grainy texture.

Two families of macroscopic cracks are visible even at low magnification. Extended planar cracks parallel to $(010)_G$ are found in all dehydrated samples and occasionally progress far beyond the reaction front in sudden events. Irregular cracks occur in some samples only and are more common where the outer surface of gypsum is slanted or rounded rather than parallel to $(010)_G$ or $(001)_G$.

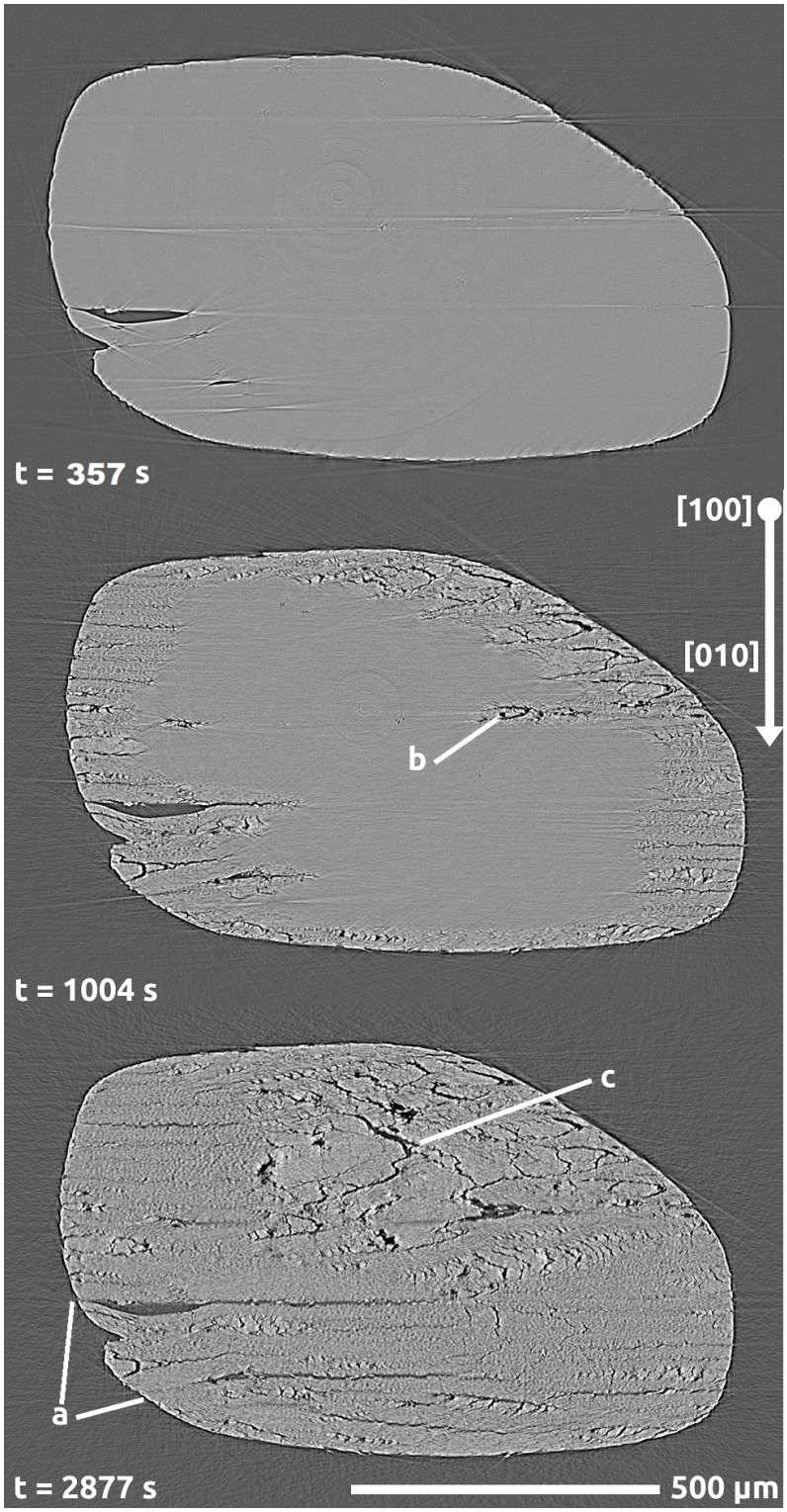

Fig. 4. X-ray absorption cross-section of the same sample before, during and after dehydration (120 °C / 20 hPa). Dehydrated areas appear in a rough texture. Most macroscopic cracks are planar and parallel to $(010)_G$ (a), sometimes extending beyond the

reaction front during dehydration (b). Irregular cracks usually occur where the outer surface is slanted or rounded (c).

Cross-sections taken on several orientations (Fig. 5) show that anhydrite is finely divided into acicular domains parallel to $[101]_G$, comparable to previous results by Sipple *et al.* [16,23]. The needle blocks are separated by marked cracks on $(010)_G$, with a consistent 3 µm width along $[010]_G$. Their width along $[10\text{-}1]_G$ ranges from 4 to 8 µm with a high variability between neighboring needles, and cracks parallel to $(10\text{-}1)_G$ are difficult to observe. While the needles are 30 to 300 µm long, there is no long-range organization along either [010] or [10-1].

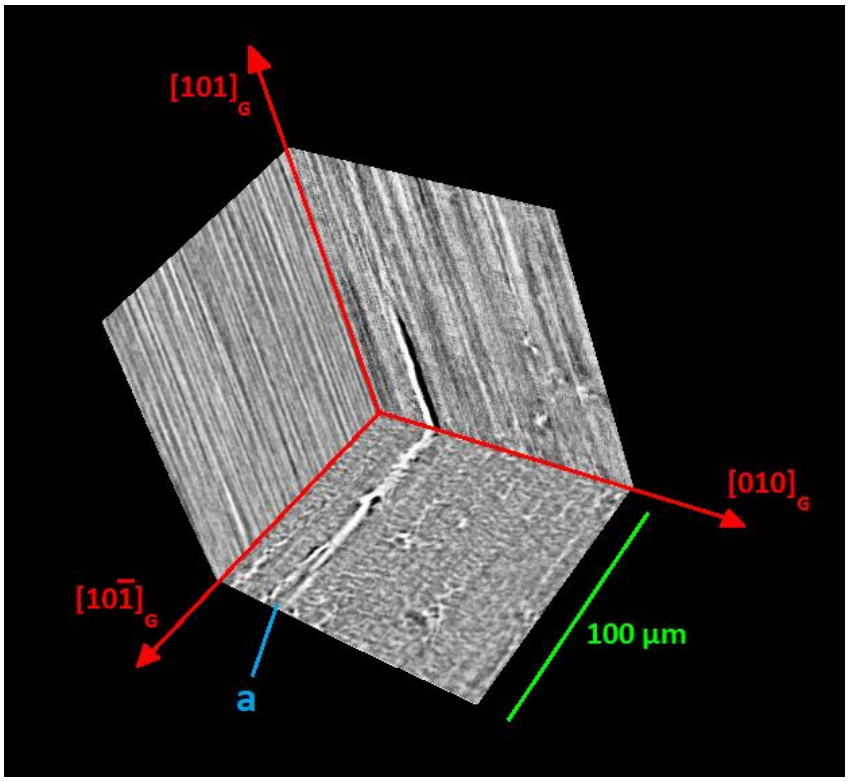

Fig. 5. X-ray microtomography cross-sections along $(10\text{-}1)_G$, $(010)_G$ and $(001)_G$. The internal microstructure of dehydrated gypsum is made of needle-shaped domains parallel to $[101]_G$. macroscropic cracks (a) are found along $(010)_G$.

Scanning electron micrographs taken on $(010)_G$ internal surfaces confirm the formation of acicular anhydrite domains. They also show that the needles are made of anhydrite crystals arranged in highly regular fishbone patterns (Fig. 6), confirming previous observations by Takahashi *et al.* [25]. The fishbone patterns are formed at an angle of 40-50 ° to the needles' axis but their crystal orientation could not be determined due to the coarse microstructure at this scale.

No further division was observed by SEM below the micron scale, which seems to contradict previous reports of self-similar microstructures down to the nanometer scale [16,23,24]. However, these may only occur in extreme conditions of temperature and water vapor partial pressure.

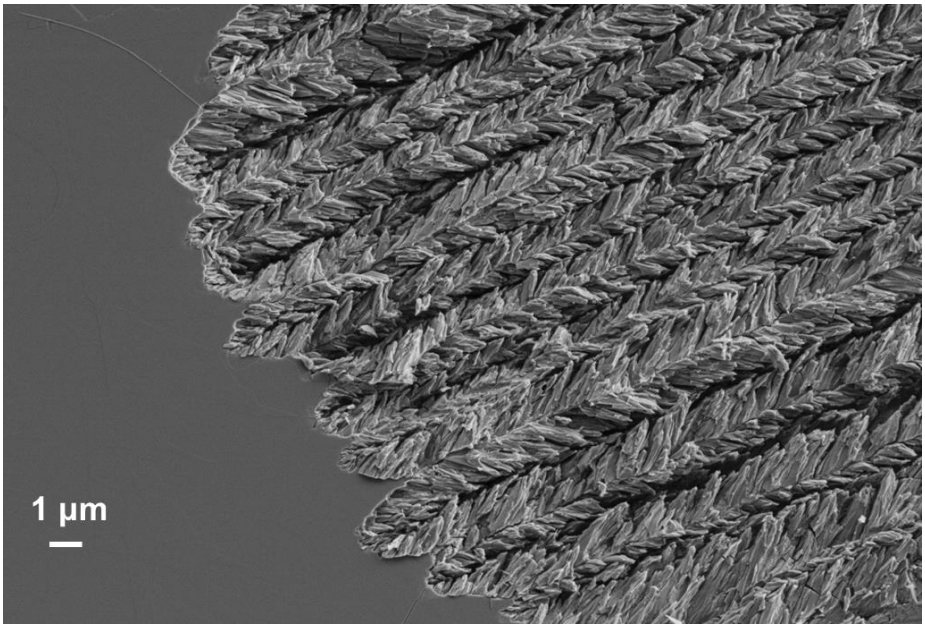

Fig. 6. SEM image of a partly dehydrated gypsum crystal, cleaved along (010) to reveal internal microstructure. Arrays of thin anhydrite crystals arranged in fishbone patterns form the µm-sized needles that can be seen with X-ray tomography.

Optical micrographs of the $(010)_G$ outer surfaces reveal the formation of hourglass figures with a typical size ranging from 10 to 100 µm (Fig. 7). These are not crystals but rather dehydrated areas. Indeed, the dark "X" figures appear to be cracks rather than crystal edges. Hourglasses are also an order of magnitude wider than individual anhydrite needles that can be seen as a striated pattern contrasting with unreacted gypsum. The length of the hourglasses, on the other hand, is an order of magnitude smaller than that of internal needles, indicating that the hourglasses are only formed at the surface of gypsum samples.

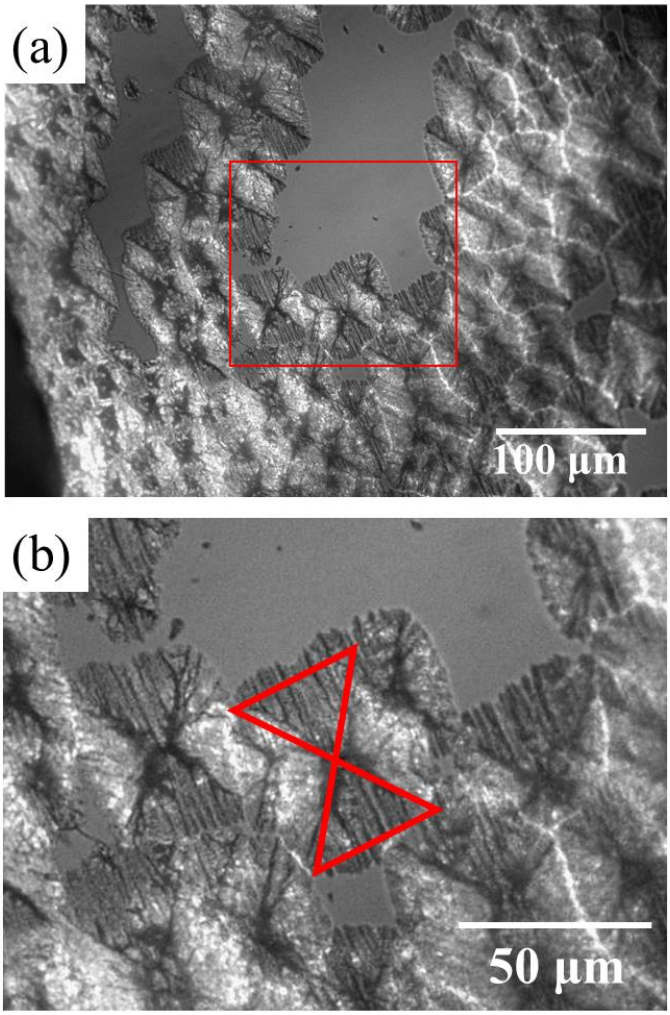

Fig. 7. Partly dehydrated gypsum crystal, observed by optical microscopy on a (010) face. The "hourglass" figures (highlighted in red) are not crystals but dehydrated areas. Shrinkage cracks show in a darker color; anhydrite needles can be seen as parallel stripes in the reacted hourglasses.

3.2 Mechanisms

Shrinkage has been proposed [16,23] as the mechanism leading to the formation of cracks in dehydrated gypsum. Axes $[010]_G$ and $[10\text{-}1]_G$ which undergo contraction indeed match with the orientation of the observed major, open cracks that extend perpendicular to those axes. These cracks lead to the formation of needles parallel to $[101]_G$ which is the only crystallographic direction free of shrinkage.

The fine division of the needles themselves however, does not result from shrinkage (as there is no shrinkage along the $[101]_G$ axis of needles). Instead, we suggest that it is a consequence of the compressive stress along $[101]_G$, caused by the increased $Ca\text{-}SO_4$ unit length in anhydrite. This compressive stress can be released by a combination of shear and rotation of crystals along cleaving planes (Fig. 8), which negates any increase of length along $[010]_G$.

The cleaving of anhydrite happens in twin orientations. Accordingly, the shear and rotation take place in two opposite directions (Fig. 8c). At the sample's surface, mechanical stress may instead be released by bending perpendicular to the surface, which is why the needles are only observed as an internal microstructure.

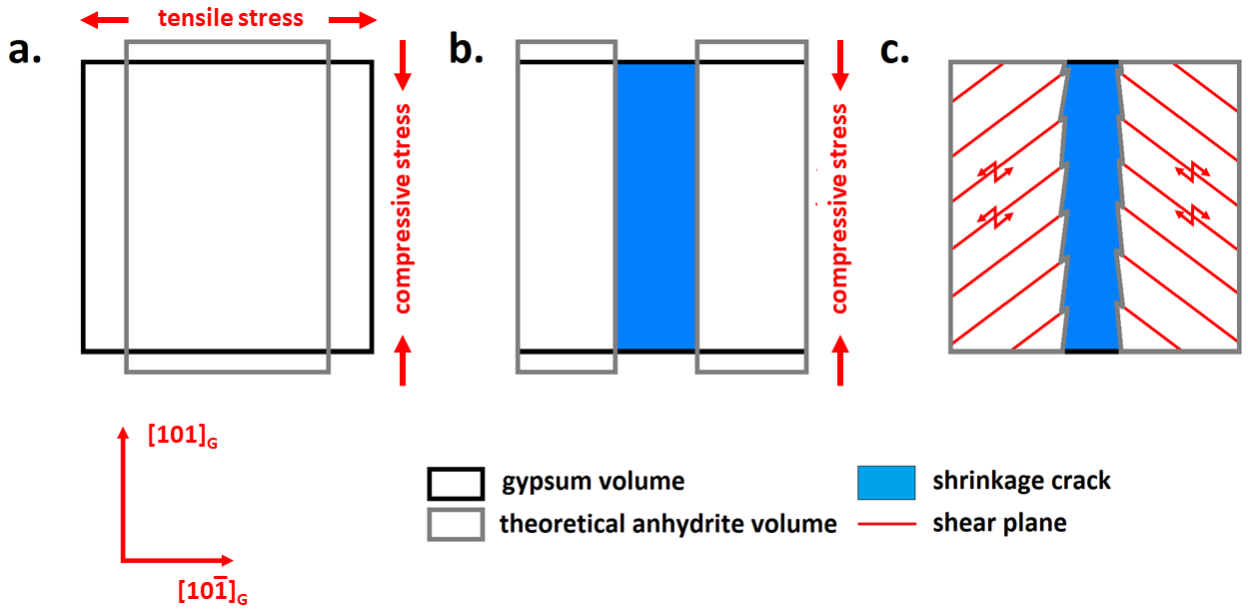

Fig. 8. Internal anhydrite growth results in opposite deformations (a). While shrinkage along $[10\text{-}1]_G$ opens wide cracks (b), compressive stress due the $[101]_G$ elongation cannot be released by homogeneous deformation due the surrounding gypsum crystal, but instead through shearing and rotation of cleaved crystals (c). Microstructural transformations are exaggerated for illustration.

3.3 Hierarchy of scales and chronology of microstructural modifications

It appears that the microstructure follows a hierarchy of scales (Fig. 9). The first scale is that of macroscopic cracks that only occur along $(010)_G$. The second scale is that of narrower cracks parallel to either $(010)_G$ or $(10\text{-}1)_G$: they extend over long distances along $[101]_G$ but not in the $(101)_G$ plane. The third scale is that of the shear cracks in fishbone patterns, that do not extend beyond the width of a single anhydrite needle.

This hierarchy is significant for two reasons. First, it closely follows the hierarchy of strengths in gypsum's chemical bonds. Macroscopic cracks of the first scale, parallel to $(010)_G$, cut across the weak hydrogen bonds that tie together the stacked planes of the structure. Cracks of the second scale break both the hydrogen bonds and the stronger ionic bonds that connect the Ca-SO_4- chains. Finally, the strongest bonds found along the $[101]_G$ axis of the chains are only broken up by the short-range cracks of the third scale.

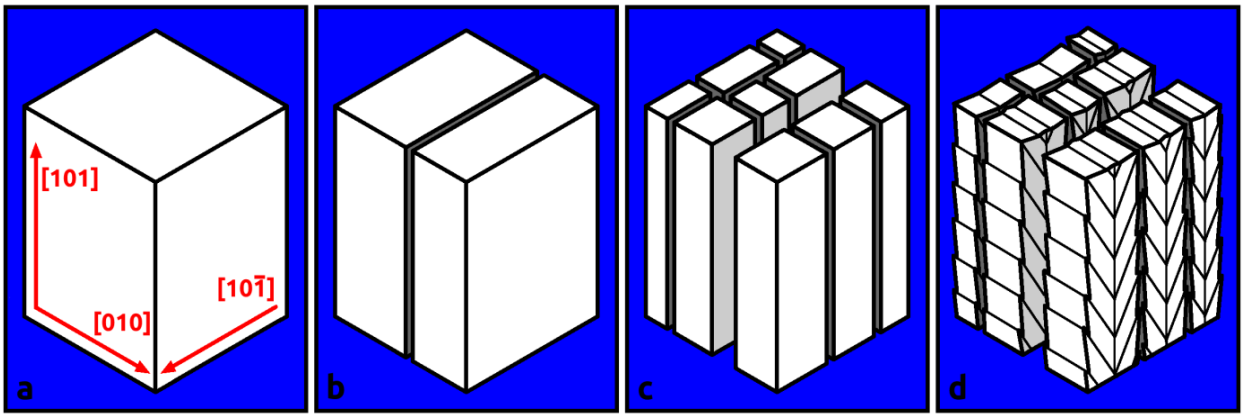

Fig. 9. Chronology of microstructural modifications resulting from the dehydration of a small internal volume of gypsum (a). Planar cracks parallel to $(010)_G$ appear (b) beyond the reaction edge. The reaction itself induces shrinkage cracks parallel to $(010)_G$ and $(10\text{-}1)_G$, forming needles of anhydrite along $[101]_G$ (c). Mechanical stress is finally released by the breakup of needles in a fishbone pattern (d). Microstructural transformations are exaggerated for illustration.

Second, the hierarchy of cracks reveals the order in which they form. Images taken at different times only show the advance of the reaction front and not how the microstructure is formed as the timescale of tomographic imaging is much longer than that of the dehydration reaction. However, cracks can only propagate in a solid material, and when several families of (even slightly) open cracks appear in succession, the growth of newer cracks stops as they intercept older cracks. By considering which family of cracks limits the extension of others, we were able to reconstruct the chronology of microstructural modifications:

- Macroscopic cracks appear first in the $(010)_G$ weak planes, even before the dehydration of gypsum, as evidenced by the fact that they occasionally propagate far beyond the reaction front (Fig. 9b).
- Criss-crossed shrinkage cracks parallel to $(010)_G$ and $(10\text{-}1)_G$ appear simultaneously as gypsum dehydrates (Fig. 9c), slicing the crystal into anhydrite needles unlimited following $[101]_G$, insofar as the Ca-SO_4- chains remain unbroken.
- Fishbone patterns only appear after the needles have formed (Fig. 9d) as there is no continuity between the patterns of neighboring needles. This supports the hypothesis that they allow the release of mechanical stress after the dehydration is locally completed and shrinkage cracks have formed.

The relative strengths of chemical bonds in the structure of gypsum are reflected in this chronology, with weaker bonds breaking up before stronger bonds; the chronology, in turn, controls the morphology of the dehydrated material. Therefore, it appears that the complex microstructures observed in dehydrated gypsum directly stem from its crystal structure.

In terms of mechanical evolution of the crystals during dehydration, there are similarities with the shrinkage cracks in drying muds. When a film of slurry dries the cracks can create rectilinear or "laddering" patterns. Early, parallel cracks divide the slurry in strips [33]. The strips are then divided by criss-crossed secondary cracks as they thoroughly dry further. The secondary cracks connect with early cracks in so-called T-junctions [34], similar to what is drawn in figure 9c. Mud cracks, however, do not follow specific orientations: the

geometry is dominated by stress while in gypsum it is dominated by the different strengths along different crystal axes.

3.4 Conditions of formation

Similar microstructures are seen in all samples, in spite of the various conditions of temperature and water vapor partial pressure. No differences are to be found with regard to the shape and orientation of cracks and anhydrite domains. The mechanisms of dehydration and microstructural modifications are therefore the same through the range of temperature and water vapor partial pressure of this study.

No variation in the typical size of the microstructure is visible to the naked eye, but a positive correlation was measured between water vapor partial pressure and typical microstructure sizes using grayscale dispersion as an indirect estimator (Fig. 10).

No correlation between temperature and microstructure size was recorded, but such an effect cannot be excluded considering that the conditions of dehydration were limited by experimental constraints. Furthermore, the chosen range of parameters only led to the formation of *β*-plasters, and the dehydration of gypsum may follow a different behavior when conducted at higher vapor partial pressures leading to the formation of *α*-plasters.

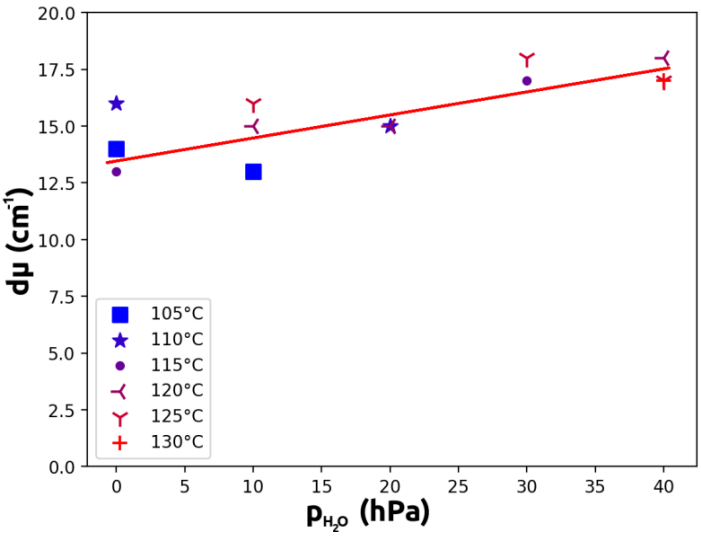

Fig. 10. Grayscale dispersion (and thus microstructure size) is linearly correlated with water vapor partial pressure ($d\mu$ = 14.1 + 0.085 p_{H2O} ; r^2 = 0.61). No such correlation is observed with temperature.

As the samples are not deformed macroscopically during the reaction (as measured quantitatively by image processing), it appears that the shrinkage and expansion induced by the dehydration of gypsum are entirely relaxed by microscopic transformations. The same microstructures should be observed regardless of the sample's size or shape. However, different behaviors may be observed when dehydrating polycrystalline or microcrystalline gypsums, especially when crystal size is near or below the typical scale of the microstructures described in this study.

4. Conclusion

The microstructures formed by the dehydration of gypsum under controlled conditions of temperature and water vapor partial pressure were characterized using in situ X-ray microtomography and post-mortem imaging by both optical and scanning electron microscopy. Complex patterns are observed, with a hierarchy that reflects the chronological steps: the largest macroscopic features are shrinkage cracks parallel to $(010)_G$ that form first and sometimes propagate beyond the reaction edge, then further dehydration results in a secondary network of narrow cracks that splits the slabs parallel to the $(010)_G$ and $(10\text{-}1)_G$ planes, cutting needles 30-300 µm long following $[101]_G$ and 4-8 x 3 µm broad following respectively $[10\text{-}1]^*_G$ and $[010]^*_G$. These domains split in turn into small crystals arranged in fishbone patterns.

All the microstructural modifications accompanying gypsum's dehydration appear to stem from a single mechanism at the atomic level. The leaving of the water molecules from the interlayers induces directly a shrinkage along $[010]_G$ and in an indirect way following $[10\text{-}1]_G$ through the re-organization of the $CaSO_4$ layers. While the strong Ca-SO_4- chains remain unbroken in the process, they faintly stretch, conceivably as a result of the redistribution of the bond strengths around the Ca^{2+} cation.

Although the same behavior was observed in all samples dehydrated at temperatures ranging from 105 to 130 °C and water vapor partial pressures ranging from 0 to 40 hPa, a moderate increase of the typical microstructure size was noted with increasing vapor partial pressures, while no such effect was recorded with temperature.

However, the parameter space explored was limited, both in temperature and in water vapor partial pressures. Further work will be necessary to investigate the dehydration of gypsum in a wider range of parameters, especially in the higher vapor pressure domain that commonly yields *α* plasters.

Future work should also investigate how the microstructures of dehydrated gypsum affect the behavior of the plaster powder during the wetting and setting of plaster. Thanks to the new knowledge of the microstructures created by the dehydration of gypsum, it is now possible to study or model the ingress of water through the network of pores and dissolution of the plaster powder, in order to determine the underlying physical mechanisms down to the scale of the nanometer.

Acknowledgements

The authors gratefully thank Elodie Boller and the staff at ESRF ID19 as well as APS 2-BM for the help with tomography experiments (during Beamtime IN1072).

This project was funded by LabEx MATISSE and Saint-Gobain Research Paris.

Authors contributions

FB: conceptualization, methodology, software, investigation, formal analysis, data curation, visualization; JDGP: investigation, visualization; FF: resources, methodology, validation; EG: conceptualization, resources, methodology, software, formal analysis; SG: resources, project administration, funding acquisition; GW: investigation, formal analysis, visualization, supervision, funding acquisition. Original draft by FB; all the co-authors contributed to writing and review.

References

[1] S. D. M. Jacques, A. G. Gonzalez-Saborido, O. Leynaud, J.-B. Bensted, M. Tyrer, R. I. W. Greaves, P. Barnes, Structural evolution during the dehydration of gypsum materials, Min. Mag. 73 (2009) 421-432, 2009.
https://doi.org/10.1180/minmag.2009.073.3.421

[2] M. Oetzel, G. Heger, T. Koslowski, Influence of ambient moisture and temperature on the phase transitions in the $CaSO_4$-H_2O system - a contribution to the production of single-phase binders from FGD gypsum, Z.K.G. Int. 53 (2000) 354-361.

[3] E. Badens, P. Llewellyn, J.-M. Fulconis, C. Jourdan, S. Veesler, R. Boistelle, F. Rouquerol, Study of Gypsum Dehydration by Controlled Transformation Rate Thermal Analysis (CRTA), J. Solid State Chem. 139 (1998) 37-44.
https://doi.org/10.1006/jssc.1998.7797

[4] J. G. D. Preturlan, L. Vieille, S. Quiligotti, L. Favergeon, Comprehensive Thermodynamic Study of the Calcium Sulfate-Water Vapor System. Part 1: Experimental Measurements and Phase Equilibria, Ind. Eng. Chem. Res. 58 (2019) 9596–9606.
10.1021/acs.iecr.9b00857

[5] J. Adrien, S. Meille, S. Tadier, E. Maire, L. Sasaki, In-situ X-ray tomographic monitoring of gypsum plaster setting, Cement Concrete Res. 82 (2016) 107-116.
10.1016/j.cemconres.2015.12.011

[6] S. Joiret, F. Pillier, A. Lemarchand, Submicrometric Picture of Plaster Hydration: Dynamic and Space-Resolved Raman Spectroscopy versus Kinetic Monte Carlo Simulations, Phys. Chem. C 118 (2014) 28730-28738.
https://doi.org/10.1021/jp510114j

[7] S. Follner, A. Wolter, K. Helming, C. Silber, H. Bartels, H. Follner, On The Real Structure of Gypsum Crystals, Crys. Res. Technol. 37 (2002) 207-218.
https://doi.org/10.1002/1521-4079(200202)37:2/3<207::AID-CRAT207>3.0.CO;2-L

[8] B. F. Pedersen, D. Semmingsen, Neutron diffraction refinement of the structure of gypsum, $CaSO_4 \cdot 2H_2O$, Acta Crystallogr. B38 (1982) 1074-1077.
https://doi.org/10.1107/S0567740882004993

[9] P. Comodi, S. Nazzareni, P. F. Zanazzi, S. Speziale S, High-pressure behavior of gypsum: A single-crystal X-ray study, Am. Mineralog. 93 (2008) 1530-1537.
https://doi:10.2138/am.2008.2917

[10] K. S. Knight, I. C. Stretton, P. F. Schofield, Temperature evolution between 50 K and 320 K of the thermal expansion tensor of gypsum derived from neutron powder, Phys. Chem. Miner. 26 (1999) 477-483.
https://doi:10.1007/S002690050210

[11] C. Bezou, A. Nonat, J.-C. Mutin, A. Nørlund Christensen, M. S. Lehmann, Investigation of the crystal structure of γ-$CaSO_4$, $CaSO_4 \cdot 0.5H_2O$ and $CaSO_4 \cdot 0.6H_2O$ by powder diffraction methods, J. Solid State Chem. 117 (1995) 165-176.
https://doi:10.1006/JSSC.1995.1260

[12] P. Ballirano, A. Maras, S. Meloni, R. Caminiti, The monoclinic I2 structure of bassanite, calcium sulphate hemihydrate, Eur. J. Mineral. 13 (2001) 985-993.
doi:10.1127/0935-1221/2001/0013/0985

[13] H. Schmidt, I. Paschke, D. Freyer, W. Voigt, Water channel structure of bassanite at high air humidity, Acta Crystallogr. B67 (2011) 467-475.
doi:10.1107/s0108768111041759

[14] G. A. Lager, T. Armbruster, F. J. Rotella, J. D. Jorgensen, D. G. Hinks, A crystallographic study of the low-temperature dehydration products of gypsum $CaSO_4 \cdot 2H_2O$: hemihydrate $CaSO_4 \cdot 0.50H_2O$, and gamma-$CaSO_4$, Am. Mineralog. 69 (1984) 910-918.

[15] A. Christensen, M. Olesen, Y. Cerenius, T. Jensen, Formation and transformation of five different phases in the $CaSO_4$-H_2O system: crystal structure of the subhydrate beta-$CaSO_4 \cdot 0.50H_2O$ and soluble anhydrite $CaSO_4$, Chem. Mater. 20 (2008) 2124-2132.
DOI:10.1039/b913648g

[16] E.-M. Sipple, P. Bracconi, P. Dufour, J.-C. Mutin, Microstructural modifications resulting from the dehydration of gypsum, Solid State Ionics 141–142 (2001) 447-454.
DOI:10.1016/S0167-2738(01)00755-X

[17] F. Fusseis, C. Schrank, J. Liu, A. Karrech, S. Llana-Fúnez, X. Xiao, K. Regenauer-Lieb, Pore formation during dehydration of a polycrystalline gypsum sample observed and quantified in a time-series synchrotron X-ray micro-tomography experiment, Solid Earth 3 (2012) 71-86.
https://doi.org/10.5194/se-3-71-2012

[18] S. Follner, A. Wolter, A. Preusser, S. Indris, C. Silber, H. Follner, The Setting Behaviour of *α*- and *β*- $CaSO_4 \cdot 0.5H_2O$ as a Function of Crystal Structure and Morphology, Cryst. Res. Technol. 37 (2002) 1075-1087.
https://DOI:10.1002/1521-4079(200210)37:10<1075::AID-CRAT1075>3.0.CO;2-X

[19] A. Fowler, H. G. Howell, K. K. Schiller, The dihydrate-hemihydrate transformation in gypsum, J. Appl. Chem. 18 (1968) 366-372.
https://doi.org/10.1016/S0022-0248(08)80092-9

[20] K. Momma, F. Izumi, VESTA 3 for three-dimensional vizualization of crystal, volumetric anc morphology data, J. Appl. Crystallogr. 44 (2011) 1272-1276.
https://doi.org/10.1107/S0021889811038970

[21] P. Ballirano, E. Melis, Thermal behaviour and kinetics of dehydration of gypsum in air from in situ real-time laboratory parallel-beam X-ray powder diffraction, Phys. Chem. Mater. 36 (2009) 391-402.
https://doi.org/10.1007/s00269-008-0285-8

[22] M. Carbone, P. Ballirano, R. Caminiti, Kinetics of gypsum dehydration at reduced pressure: an energy dispersive X-ray diffraction study, Eur. J. Mineral. 20 (2008) 621-627.
DOI:10.1127/0935-1221/2008/0020-1826

[23] E.-M. Sipple, P. Bracconi, P. Dufour, J.-C. Mutin, Electronic microdiffraction study of structural modifications resulting from the dehydration of gypsum. Prediction of the microstructure of resulting pseudomorphs, Solid State Ionics 141–142 (2001) 455-461. DOI:10.1016/S0167-2738(01)00755-X

[24] C. Sella, M.-F. Sella, Etude de la déshydratation du gypse, J. Microsc. Fr. 1 (1962) 215-26.

[25] S. Takahashi, K. Setoyama, SEM observation of *β*-calcium sulfate hemihydrate particles II. Effects of raw gypsum and condition of production on internal microstructure, Gypsum and Lime 220 (1989) 135-141. https://doi.org/10.11451/mukimate1953.1989.135

[26] L. de Lapparent, Précis de Minéralogie, Masson et C. Ed., Paris (1921) 257.

[27] P. Berger, B. Gilles, H. Buscail, S. Chevalier, H. Evin, L. Favergeon, O. Heintz, C. Issartel, V. Ji, L. Martinelli, Tools for Studying Water Vapor at High Temperatures, French Activity High Temperature Corrosion in Water Vapor, Trans Tech Publications (2014) 152–154.

[28] T. Weitkamp, P. Tafforeau, E. Boller, P. Cloetens, J.-P. Valade, P. Bernard, F. Peyrin, W. Ludwig, L. Helfen, J. Baruchel, Status and evolution of the ESRF beamline ID19, AIP Conference Proceedings 1221:1 (2010) 33-38.

[29] T. Weitkamp, P. Tafforeau, E. Boller, P. Cloetens, J.-P. Valade, P. Bernard, F. Peyrin, W. Ludwig, L. Helfen, J. Baruchel, Parallel-beam imaging at the ESRF beamline ID19: current status and plans for the future, AIP Conference Proceedings 1234:1 (2010) 83-86.

[30] A. Mirone, E. Gouillart, E. Bruna, P. Tafforeau, J. Kieffer, PyHST2 Hybrid distributed code for high speed tomographic reconstruction with iterative reconstruction and a priori knowledge capabilites, Nuclear Instrum. Methods B 324 (2014) 41-48. https://doi:10:1016/j.nimb.2013.09.030

[31] E. Gouillart, J. Nunez-Iglesias, S. Van der Walt, Analyzing microtomography data with Python and the scikit-image library, Advanced Structural and Chemical Imaging 2 (2017) 18. https://doi.org/10.1186/s40679-016-0031-0

[32] S. Van der Walt, J.-L. Schönberger, J. Nunez-Iglesias, F. Boulogne, J.-D. Warner, N. Yager, E. Gouillart, T. Yu, Scikit-image: image processing in Python, PeerJ 2 (2014) 453. doi:10.7717/peerj.453

[33] K. A. Shorlin, J. R. de Bruyn, M. Graham, S. W. Morris, Development and geometry of isotropic and directional shrinkage crack patterns, Phys. Rev. E 61 (2000) 6950–6957. doi: 10.1103/physreve.61.6950.

[34] L. Goehring, R. Conroy, A. Akhter, W. J. Clegg, A. F. Routh, Evolution of mud-crack patterns during repeated drying cycles, Soft Matter 6 (2010) 3562–3567. https://doi.org/10.1039/B922206E